Dispersion of polarization coupling, localized and collective plasmon modes in a metallic photonic crystal mapped by Mueller Matrix Ellipsometry

Thomas Brakstad,[1] **Morten Kildemo,**[1,2] **Zahra Ghadyani,**[1] **and Ingve Simonsen**[1,3]

[1]*Department of Physics, Norwegian University of Science and Technology, NO-7491 Trondheim, Norway*
[2]*morten.kildemo@ntnu.no*
[3]*ingve.simonsen@ntnu.no*

Abstract: We report a spectroscopic Mueller matrix experimental study of a plasmonic photonic crystal consisting of gold hemispheroidal particles (lateral radius 54 nm, height 25 nm) arranged on a square lattice (lattice constant 210 nm) and supported by a glass substrate. Strong polarization coupling is observed for ultraviolet wavelengths and around the surface plasmon resonance for which the off-block-diagonal Mueller matrix elements show pronounced anisotropies. Due to the Rayleigh anomalies, the block-diagonal Mueller matrix elements produce a direct image of the Brillouin Zone (BZ) boundaries of the lattice and resonances are observed at the M-point in the first and at the X-point in the second BZ. These elements show also the dispersion of the localized surface plasmon resonance.

OCIS codes: (240.6680) Surface plasmons; (120.2130) Ellipsometry and polarimetry; (160.4236) Nanomaterials; (290.5855) Scattering, polarization.

References and links

1. T. Oates, H. Wormeester, and H. Arwin, "Characterization of plasmonic effects in thin films and metamaterials using spectroscopic ellipsometry," Prog. Surf. Sci. **86**, 328–376 (2011).
2. F. Monticone and A. Alù, "Metamaterials and plasmonics: From nanoparticles to nanoantenna arrays, metasurfaces, and metamaterials," Chinese Physics B **23**, 047809 (2014).
3. S. Maier, *Plasmonics: Fundamentals and Applications* (Springer, 2007).
4. R. A. Shelby, D. R. Smith, and S. Schultz, "Experimental verification of a negative index of refraction," Science **292**, 77–79 (2001).
5. N. Fang, H. Lee, C. Sun, and X. Zhang, "Sub-diffraction-limited optical imaging with a silver superlens," Science **308**, 534–537 (2005).
6. K. Busch, S. Lölkes, R. Wehrspohn, and H. Föll, *Photonic Crystals: Advances in Design, Fabrication, and Characterization* (Wiley, 2006).
7. L. M. S. Aas, M. Kildemo, C. Martella, M. C. Giordano, D. Chiappe, and F. B. de Mongeot, "Optical properties of biaxial nanopatterned gold plasmonic nanowired gridpolarizer," Opt. Express **21**, 30918–30931 (2013).
8. T. W. H. Oates, M. Ranjan, S. Facsko, and H. Arwin, "Highly anisotropic effective dielectric functions of silver nanoparticle arrays." Opt. Express **19**, 2014–2028 (2011).
9. M. Ranjan, T. W. H. Oates, S. Facsko, and W. Möller, "Optical properties of silver nanowire arrays with 35 nm periodicity." Opt. Lett. **35**, 2576–2578 (2010).
10. N. Guth, B. Gallas, J. Rivory, J. Grand, A. Ourir, G. Guida, R. Abdeddaim, C. Jouvaud, and J. de Rosny, "Optical properties of metamaterials: Influence of electric multipoles, magnetoelectric coupling, and spatial dispersion," Phys. Rev. B **85**, 115138 (2012).

#240547 Received 7 May 2015; revised 3 Aug 2015; accepted 16 Aug 2015; published 21 Aug 2015

11. D. Schmidt, B. Booso, T. Hofmann, E. Schubert, A. Sarangan, and M. Schubert, "Generalized ellipsometry for monoclinic absorbing materials: determination of optical constants of cr columnar thin films," Opt. Lett. **34**, 992–994 (2009).
12. G. K. Larsen and Y. Zhao, "Extracting the anisotropic optical parameters of chiral plasmonic nanostructured thin films using generalized ellipsometry," Applied Physics Letters **105**, 071109 (2014).
13. V. G. Kravets, F. Schedin, and A. N. Grigorenko, "Extremely narrow plasmon resonances based on diffraction coupling of localized plasmons in arrays of metallic nanoparticles," Phys. Rev. Lett. **101**, 087403 (2008).
14. B. Lamprecht, G. Schider, R. T. Lechner, H. Ditlbacher, J. R. Krenn, A. Leitner, and F. R. Aussenegg, "Metal nanoparticle gratings: Influence of dipolar particle interaction on the plasmon resonance," Phys. Rev. Lett. **84**, 4721–4724 (2000).
15. D. Bedeaux and J. Vlieger, *Optical Properties Of Surfaces*, 2nd edition (World Scientific Publishing Company, 2004).
16. H. G. Tompkins and E. A. Irene, *Handbook of Ellipsometry* (William Andrew Inc., 2005).
17. H. Fujiwara, ed., *Spectroscopic Ellipsometry: Principles and Applications* (John Wiley & Sons Ltd., 2007).
18. P. C. Wu, T.-H. Kim, A. S. Brown, M. Losurdo, G. Bruno, and H. O. Everitt, "Real-time plasmon resonance tuning of liquid Ga nanoparticles by in situ spectroscopic ellipsometry," Appl. Phys. Lett. **90**, 103119 (2007).
19. L. Aas, M. Kildemo, Y. Cohin, and E. Søndergård, "Determination of small tilt angles of short gasb nanopillars using uv-visible Mueller matrix ellipsometry," Thin Solid Films **541**, 97–101 (2012).
20. Z. Ghadyani, M. Kildemo, L. M. S. Aas, Y. Cohin, and E. Søndergård, "Anisotropic plasmonic cu nanoparticles in sol-gel oxide nanopillars studied byspectroscopic Mueller matrix ellipsometry," Opt. Express **21**, 30796–30811 (2013).
21. R. Lazzari and I. Simonsen, "GranFilm: a software for calculating thin-layer dielectric properties and Fresnel coefficients," Thin Solid Films **419**, 124–136 (2002).
22. R. Lazzari, J. Jupille, R. Cavallotti, and I. Simonsen, "Model-free unraveling of supported nanoparticles plasmon resonance modes," J. Phys. Chem. C **118**, 7032–7048 (2014).
23. R. Azzam and N. Bashara, *Ellipsometry and Polarized Light* (North-Holland, 1977).
24. M. Schubert, "Polarization-dependent optical parameters of arbitrarily anisotropic homogeneous layered systems," Phys. Rev. B **53**, 4265–4274 (1996).
25. M. Schubert, "Theory and Application of Generalized Ellipsometry" in *Handbook of Ellipsometry*, H. G. Tompkins and E. A. Irene, eds. (Springer, 2005).
26. P. S. Hauge, R. H. Muller and C. G. Smith, "Conventions and formulas for using the Mueller-Stokes calculus in ellipsometry," Surf. Sci. **96**, 81–107 (1980).
27. P. A. Letnes, A. A. Maradudin, T. Nordam, and I. Simonsen, "Calculation of all elements of the Mueller matrix for scattering of light from a two-dimensional randomly rough metal surface," Phys. Rev. A **86**, 031803(R) (2012).
28. I. Simonsen, R. Lazzari, J. Jupille, and S. Roux, "Numerical modeling of the optical response of supported metallic particles," Phys. Rev. B **61**, 7722–7733 (2000).
29. M. Losurdo, M. M. Giangregorio, G. V. Bianco, A. A. Suvorova, C. Kong, S. Rubanov, P. Capezzuto, J. Humlicek, and G. Bruno, "Size dependence of the dielectric function of silicon-supported plasmonic gold nanoparticles," Phys. Rev. B **82**, 155451 (2010).
30. R. Rehammar, F. A. Ghavanini, R. Magnusson, J. M. Kinaret, P. Enoksson, H. Arwin, and E. E. B. Campbell, "Electromechanically tunable carbon nanofiber photonic crystal," Nano Letters **13**, 397–401 (2013).
31. R. Rehammar, R. Magnusson, A. I. Fernandez-Dominguez, H. Arwin, J. M. Kinaret, S. A. Maier, and E. E. B. Campbell, "Optical properties of carbon nanofiber photonic crystals," Nanotechnology **21**, 465203 (2010).
32. M. Kretschmann and A. A. Maradudin, "Band structures of two-dimensional surface-plasmon polaritonic crystals," Phys. Rev. B **66**, 245408 (2002).
33. R. Lazzari, S. Roux, I. Simonsen, J. Jupille, D. Bedeaux, and J. Vlieger, "Multipolar plasmon resonances in supported silver particles: the case of Ag/α-$Al_2O_3(0001)$," Phys. Rev. B **65**, 235424 (2002).
34. G. Weick, C. Woollacott, W. L. Barnes, O. Hess, and E. Mariani, "Dirac-like plasmons in honeycomb lattices of metallic nanoparticles," Phys. Rev. Lett. **110**, 106801 (2013).
35. R. Shen, L. B. Shao, B. Wang, and D. Y. Xing, "Single Dirac cone with a flat band touching on line-centered-square optical lattices," Phys. Rev. B **81**, 041410 (2010).
36. M. G. Moharam and T. K. Gaylord, "Rigorous coupled-wave analysis of planar-grating diffraction," J. Opt. Soc. Am. **71**, 811–818 (1981).
37. M. Foldyna, A. De Martino, E. Garcia- Caurel, R. Ossikovski, C. Licitra, F. Bertin, K. Postava and B. Drevillon, "Critical dimension of biperiodic gratings determined by spectral ellipsometry and Mueller matrix polarimetry," Eur. Phys. J. Appl. Phys. **42**, 351-359 (2008).
38. I. Simonsen, A. A. Maradudin, and T. A. Leskova, "The Scattering of Electromagnetic Waves from Two-Dimensional Randomly Rough Penetrable Surfaces," Phys. Rev. Lett. **104**, 223904 (2010).
39. I. Simonsen, A. A. Maradudin, and T. A. Leskova, "The Scattering of Electromagnetic Waves from Two-Dimensional Randomly Rough Perfectly Conducting Surfaces: The Full Angular Intensity Distribution," Phys. Rev. A **81**, 013806 (2010).

#240547 Received 7 May 2015; revised 3 Aug 2015; accepted 16 Aug 2015; published 21 Aug 2015

40. T. Nordam, P. A. Letnes, and I. Simonsen, "Numerical simulations of scattering of light from two-dimensional rough surfaces using the reduced rayleigh equation," Front. Physics **1**, 8 (2013).
41. A. Sedghi, S. Valiaghaie, and A. Soufiani, "Detailed Study of the TE band structure of two dimensional metallic photonic crystals with square symmetry," J. Korean Phys. Soc.**65**, 1020–1023 (2014).
42. A. S. Vala, S. R. Entezar, and A. A. Sedghi, "Band structure of two-dimensional square lattice photonic crystals of circular dispersive metamaterial rods," Eur. Phys. J. B **81**, 269–274 (2011).

1. Introduction

Ellipsometric characterization of plasmonic nanoparticles on surfaces is an interesting problem dating back to the original works of Drude [1]. New nanofabrication methods make it possible to produce highly ordered plasmonic surfaces and thereby plasmonic metamaterial surfaces and materials with predefined structures, revealing new optical properties [2, 3]. It is expected that generalized or Mueller matrix ellipsometry can play an important role in the characterization of such plasmonic metamaterials [1], with their fascinating properties such as e.g. negative refractive index [4] and its application to perfect lensing and subdiffraction imaging [5]. However, within the limitations of nanofabrication, the macroscopic effective properties of metamaterials and even arrays of plasmonic particles, share many features with photonic crystals [2], and it is necessarily the combined response that will be observed by spectroscopy across a larger spectral range.

The fields of plasmonics [3] and plasmonic metamaterials [2] have been booming in recent years in terms of the number of conducted theoretical/numerical and experimental studies and in terms of applications. Up till now, the majority of the experimental efforts have focused on reflection or transmission measurements using either p- or s-polarized illumination and detecting the co-polarized reflected or transmitted light [3, 6]. Therefore, the *polarization coupling*, and the vast information that may be derived from it, has for the most part simply been neglected. The importance of the polarization coupling can be directly observed in Mueller matrix spectroscopic studies with complete azimuthal sample rotation of inherently anisotropic systems, such as self-assembled Ag or Au particles along the ripples of a nanopatterned substrate [7–9], meta-surfaces of U-shaped particles [10], slanted metallic pillars [11], and chiral structures [12]. For highly ordered arrays of plasmonic/metallic particles, the lattice plays a major role, and a number of reports show experimentally and numerically that the localized surface plasmon resonance (LSPR) is strongly perturbed by the Rayleigh/Wood modes that occurs in photonic crystals [6, 13], i.e. for lattice constants with nominally weak dipole-dipole interactions [14]. For lattice constants in the near field regime dominated by dipole-dipole interaction [3], the LSPR can be well described by the quasi-static approximation for nanosized islands on a substrate, where the near field interaction is included between the islands in a square or hexagonal lattice, also including the induced dipoles in the substrate. The Bedeaux-Vlieger model [15] is such a method, but it does not take into account polarization coupling, and hence result in block-diagonal Mueller matrices. However, the plasmon modes occurring as a result of the lattice for larger lattice constants, can be expected to both convey polarization coupling and resonances not accounted for in the Bedeaux-Vlieger model, and also reflect the two-dimensional photonic crystal character of the surface. Previous experimental work exploring generalized ellipsometry have mainly been reported using Electron Beam Lithography (EBL) combined with Ion-Beam Etching (IBE) or lift-off, where a conductive ITO layer absorbing in the ultra-violet (uv) was used between the pattern and the transparent substrate [10, 13] in order to combat substrate charging effects. Through the use of Focused Ion Beam milling (FIB) of a thin Au film, the ITO layer can be omitted, which allows to reveal the complete picture, since Rayleigh modes can then freely propagate also in the uv-range in fused-SiO_2.

Spectroscopic ellipsometry is a powerful and sensitive tool that is widely used in the monitoring and control during the manufacture of stacks of thin films and e.g. critical dimensions of

#240547 Received 7 May 2015; revised 3 Aug 2015; accepted 16 Aug 2015; published 21 Aug 2015

subwavelength gratings [16, 17]. It is also a self-referencing technique that is highly sensitive to plasmonic particles on surfaces [1], and well adapted for in-situ monitoring [18]. Recent advances in optical instrumentation allows for the measurement of the complete spectroscopic Mueller matrix in the range 0.7–5.9 eV, in less than 20 seconds, which allow for rapid mapping of the azimuthal angle dependency and the incidence angle dependency of the sample response. Furthermore, through the use of focusing probes it is possible to position the ellipsometric spot at a high angle of incidence onto a small (e.g. $200\,\mu m \times 200\,\mu m$) area and further make measurements with full azimuthal rotation of the sample [7, 19, 20]. This technique appears thus appropriate for the characterization of a range of plasmonic photonic crystal and metamaterial surfaces.

The purpose of this paper is to experimentally reveal the complete polarization response of a square lattice of plasmonic particles on uv-transparent glass, to qualitatively explain the main features of the reflected light, and to point out new effects that will be interesting to pursue further in a rigorous analysis by appropriate computational methods.

2. Experimental

The samples were produced by evaporating a thin film of Au onto a clean uv-grade fused silica surface using an e-beam evaporator (Pfeiffer Vacuum Classic 500). The evaporation was performed at a pressure of 10^{-7} Torr with an acceleration voltage of 8 kV and an electron current of approximately 38 mA, resulting in an evaporation rate of $1.7\,\text{Å}\,\text{s}^{-1}$. The resulting films were smooth, but polycrystalline. The Au nano-structures on glass were produced by FIB-milling using Ga ions (FEI Helios Dual-beam FIB) with manufacture parameters set as acceleration voltage of 50 kV, 26 pA current and milling depth of 45 nm. The initial film thickness determined by spectroscopic ellipsometry on unmilled areas was 40 nm. The sample was manufactured to make up half spheres of Au distributed in a square pattern on a glass-surface, with lattice constant $a = 210\,\text{nm}$.

After the milling, the particles were found to be shaped like hemispheroids of lateral radius (54 ± 4) nm, see the Scanning Electron Microscopy (SEM) image in Fig. 1. Atomic Force Microscopy (AFM) in contact mode (Bioscope Catalyst from Bruker, with ScanAsyst Air probe with tip radius less than 10 nm) resulted in a top-to-bottom height of 49 nm, which implies an over-etching into the substrate of at least 9 nm, i.e. the Au particles are on top a dielectric mound. This can also be observed by close inspection of the SEM image in Fig. 1, which shows that an apparent mound of approximately 75 nm radius surrounds each Au particle. Modeling of the block-diagonal Mueller matrix elements, was performed using the most recent GranFilm implementation of the Bedeaux-Vlieger model [21] for truncated spheroidal particles supported by a (flat) SiO_2 substrate. In these calculations, one neglected finite size and retardation effects in each particle, the influence of Rayleigh/Wood modes, and the SiO_2 ridge underneath each particle. By this procedure, a reasonable fit to the ellipsometric data below 2.5 eV was found for a lateral radius of 48 nm and a height of 24 nm. Furthermore, the energy position of the LSPR was found to be sensitive to small variations in the lattice constant, but the lattice constant was found to contribute more strongly to the amplitude of the resonance, i.e. to the total coverage. As a result the resulting lattice constant appears inconclusive for lattice constants larger than about 150 nm.

Additionally, correlating the AFM and the SEM images and considering tip convolution effects of the AFM, we estimated a 20–25 nm high SiO_2 mound underneath each particle, while the corresponding height of the Au particle is estimated to be in the range of 25–30 nm, respectively. The fact that the supporting substrate is not flat needs to be addressed in future rigorous models of this system.

Finally, the random deviation from spheroidal shape is believed to be mainly a result of

#240547 Received 7 May 2015; revised 3 Aug 2015; accepted 16 Aug 2015; published 21 Aug 2015

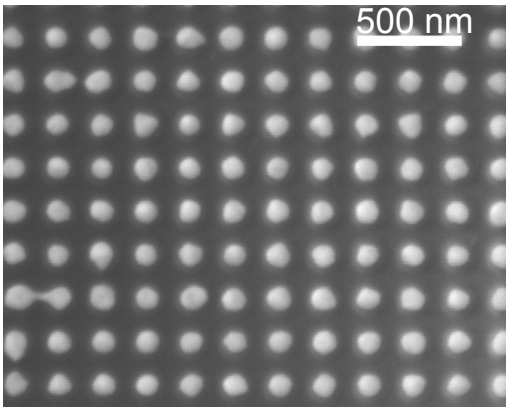

Fig. 1. SEM image of the Au nanoparticles on SiO_2 with the scale bar indicating 500 nm. The image was recorded at 15 kV with a magnification of 50 k.

the polycrystallinity of the film. Occational defects, like the one seen in the lower left corner of Fig. 1, will most likely give a negligible contribution to the overall ellipsometric response. Higher milling accuracy could be obtained, but at the expense of total manufacturing time. It is noted that for a separate sample produced on a Transmission Electron Microscopy (TEM)-grid, traces of sub-nanometer sized Au islands were observed. Such islands are probably a result of the milling process (and redeposition), but for the overall optical response of the system, we assume that they can be neglected.

For the optical characterization of the samples, a variable angle multichannel dual rotating compensator Mueller matrix ellipsometer (RC2) from JA Woollam Company was used. The instrument has a collimated 150 W Xe source and operates in the spectral range from 210 nm (5.9 eV) to 1700 nm (0.73 eV), using a combination of silicon and indium gallium arsenide spectrograph having a resolution of 1 nm below 1000 nm and 2.5 nm above. The initial collimated beam has a waist of approximately 3 mm, but in the present work focusing and collection lenses with a focal length of 20 mm and a Numerical Aperture of approximately 0.15, were applied, allowing a normal incidence spot size of less than 100 μm. This spot size allowed us to study the full azimuthal rotation of the sample while ensuring that the spot-size remained within the 240 μm × 240 μm area opened by FIB-milling. The spectroscopic Mueller matrix was measured for the incidence angles (with respect to surface normal) 45°, 55° and 65°. Full azimuthal rotation of the sample around the sample normal (360°) in steps of 5° was performed for each angle of incidence in order to fully map any anisotropy in the optical response of the sample. The sample was carefully aligned using a camera to observe the spot within the milled area, and to insure that the rotation center was a sample alignment that contained the spot within. When using focusing optics the sample alignment upon rotation is very sensitive, and was therefore adjusted prior to the measurement of each angle of incidence. The rotation stage used in these measurements did not have a translation stage, and the samples were therefore manually readjusted at each angle of incidence.

The same instrument was also used to measure the spectroscopic transmission Mueller matrix of the sample. The depolarization was used to verify if the spot was positioned properly within the sample area, as strong depolarization occurs for a beam overlapping the Au-film and the nanopatterned area. This is particularly easy in our case, since the milled sample area is surrounded by the original Au layer. No major depolarization was observed from any of the samples. Furthermore, we do not observe any additional depolarization around any of the plasmon-resonances, but we observed a small depolarization below the plasmon resonance (maximum

#240547 Received 7 May 2015; revised 3 Aug 2015; accepted 16 Aug 2015; published 21 Aug 2015

of 6 %) at the higher incidence angles. The high incidence angles (65°) showed in some cases some additional depolarization at lower energies, which is speculated to be a result of the dispersion of the focusing optics.

3. Theory

The polarization state of light reflected from the sample when described in terms of Stokes vectors, can be fully characterized by the Mueller matrix associated with the sample. The change in polarization state of monochromatic light upon reflection from a smooth surface can in the non-depolarizing case be formulated by the 2×2 complex Jones matrix transforming the incoming polarization state to the reflected polarization state by the reflection amplitudes (r_{pp}, r_{ps}, etc.) [17, 23]

$$\begin{bmatrix} E_p \\ E_s \end{bmatrix}_{\text{ref}} = \begin{bmatrix} r_{pp} & r_{ps} \\ r_{sp} & r_{ss} \end{bmatrix} \begin{bmatrix} E_p \\ E_s \end{bmatrix}_{\text{inc}}. \tag{1}$$

In writing Eq. (1), E_p and E_s have been introduced as the plane wave electric field components that are parallel and perpendicular to the plane of incident, respectively. Moreover, $\{r_{\alpha\beta}\}$ ($\alpha, \beta = p, s$) denote the reflection amplitudes for β-polarized light reflected by the sample into α-polarized light. Be aware that it is also fairly common in the literature to adopt a convention where the order of the polarization indices of the reflection amplitudes is reversed so that the first polarization index refers to the incident light (and not the reflected light, like in our case) [24, 25]. The polarization base we adopt is the right-handed $\{\hat{\mathbf{p}}, \hat{\mathbf{s}}, \mathbf{k}\}$ convention [16, 26], where $\hat{\mathbf{p}}$ and $\hat{\mathbf{s}}$ denote the unit polarization vectors for p- and s-polarized light, while $\mathbf{k}$ represents the incident or specularly reflected wave vector (so that $\hat{\mathbf{p}} \times \hat{\mathbf{s}} = \hat{\mathbf{k}}$), see Fig. 2. Moreover, the angles of incidence (θ_0, ϕ_0) and the angles of scattering (θ_s, ϕ_s) are defined as shown in Fig. 2.

For a non-depolarizing sample, we assume that the measured Mueller matrix is represented by the so-called Mueller-Jones matrix derived from the most general Jones matrix for anisotropic samples [26]:

$$\mathbf{M} = \begin{bmatrix} M_{11} & M_{12} & M_{13} & M_{14} \\ M_{21} & M_{22} & M_{23} & M_{24} \\ M_{31} & M_{32} & M_{33} & M_{34} \\ M_{41} & M_{42} & M_{43} & M_{44} \end{bmatrix}. \tag{2}$$

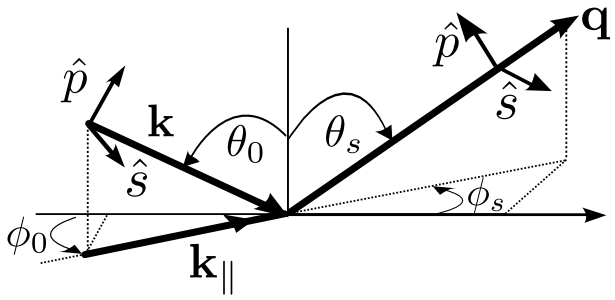

Fig. 2. Schematic diagram of the measurement geometry and the polarization base. The measurements are performed in specular reflection so that $\phi_0 = \phi_s$ and $\theta_0 = \theta_s$. It is assumed that the coordinate system is oriented so that its x- and y-axis are parallel to the two primitive translation vectors of the square lattice that the particles in Fig. 1 define.

#240547 Received 7 May 2015; revised 3 Aug 2015; accepted 16 Aug 2015; published 21 Aug 2015

The elements of $\mathbf{M}$ are given by [26, 27]:

$$M_{11} = \frac{1}{2}\left(|r_{pp}|^2 + |r_{sp}|^2 + |r_{ps}|^2 + |r_{ss}|^2\right) \tag{3a}$$

$$M_{12} = \frac{1}{2}\left(|r_{pp}|^2 + |r_{sp}|^2 - |r_{ps}|^2 - |r_{ss}|^2\right) \tag{3b}$$

$$M_{13} = \mathrm{Re}\left(r_{pp}r_{ps}^* + r_{sp}r_{ss}^*\right) \tag{3c}$$

$$M_{14} = \mathrm{Im}\left(r_{pp}r_{ps}^* + r_{sp}r_{ss}^*\right) \tag{3d}$$

$$M_{21} = \frac{1}{2}\left(|r_{pp}|^2 - |r_{sp}|^2 + |r_{ps}|^2 - |r_{ss}|^2\right) \tag{3e}$$

$$M_{22} = \frac{1}{2}\left(|r_{pp}|^2 - |r_{sp}|^2 - |r_{ps}|^2 + |r_{ss}|^2\right) \tag{3f}$$

$$M_{23} = \mathrm{Re}\left(r_{pp}r_{ps}^* - r_{sp}r_{ss}^*\right) \tag{3g}$$

$$M_{24} = \mathrm{Im}\left(r_{pp}r_{ps}^* - r_{sp}r_{ss}^*\right) \tag{3h}$$

$$M_{31} = \mathrm{Re}\left(r_{pp}r_{sp}^* + r_{ps}r_{ss}^*\right) \tag{3i}$$

$$M_{32} = \mathrm{Re}\left(r_{pp}r_{sp}^* - r_{ps}r_{ss}^*\right) \tag{3j}$$

$$M_{33} = \mathrm{Re}\left(r_{pp}r_{ss}^* + r_{ps}r_{sp}^*\right) \tag{3k}$$

$$M_{34} = \mathrm{Im}\left(r_{pp}r_{ss}^* - r_{ps}r_{sp}^*\right) \tag{3l}$$

$$M_{41} = -\mathrm{Im}\left(r_{pp}r_{sp}^* + r_{ps}r_{ss}^*\right) \tag{3m}$$

$$M_{42} = -\mathrm{Im}\left(r_{pp}r_{sp}^* - r_{ps}r_{ss}^*\right) \tag{3n}$$

$$M_{43} = -\mathrm{Im}\left(r_{pp}r_{ss}^* + r_{ps}r_{sp}^*\right) \tag{3o}$$

$$M_{44} = \mathrm{Re}\left(r_{pp}r_{ss}^* - r_{ps}r_{sp}^*\right). \tag{3p}$$

The off-block-diagonal elements of $\mathbf{M}$ represent *polarization coupling*. The Mueller matrix is conventionally normalized by the M_{11} element. Here the normalized Mueller matrix is denoted by $\mathbf{m} = [m_{ij}]$ with $m_{ij} = M_{ij}/M_{11}$ $(i, j = 1, \ldots, 4)$ so that trivially $m_{11} \equiv 1$. Hence, no reference measurement is required beyond standard calibration.

The GranFilm software [21, 28], which is based on the Bedeaux-Vlieger (BV) model [15], assumes the quasi-static approximation and uses effective boundary conditions on a flat dividing surface, and cross-polarized reflection is *not* allowed. This means that the resulting Mueller matrix will be block-diagonal and have the form

$$\mathbf{M}_{\mathrm{BV}} = \begin{bmatrix} 1 & -\mathrm{N} & 0 & 0 \\ -\mathrm{N} & 1 & 0 & 0 \\ 0 & 0 & \mathrm{C} & \mathrm{S} \\ 0 & 0 & -\mathrm{S} & \mathrm{C} \end{bmatrix}, \tag{4}$$

where $N = \cos 2\psi$, $C = \sin 2\psi \cos\Delta$ and $S = \sin 2\psi \sin\Delta$, with ψ and Δ denoting the ellipsometric angles [17, 26]. By the use of GranFilm, the quantities N, C, and S were used to estimate the topographical parameters of the samples with the results stated in Sec. 2. However, since polarization coupling was observed, the complete Jones matrix was additionally estimated by fitting it to the presumed Mueller-Jones matrix [23, 25]. This process allows for estimating the

#240547 Received 7 May 2015; revised 3 Aug 2015; accepted 16 Aug 2015; published 21 Aug 2015

generalized ellipsometric parameters [25]:

$$\rho_{pp} = \frac{r_{pp}}{r_{ss}} = \tan\psi_{pp}\, e^{\mathrm{i}\Delta_{pp}} \tag{5a}$$

$$\rho_{ps} = \frac{r_{ps}}{r_{ss}} = \tan\psi_{ps}\, e^{\mathrm{i}\Delta_{ps}} \tag{5b}$$

$$\rho_{sp} = \frac{r_{sp}}{r_{pp}} = \tan\psi_{sp}\, e^{\mathrm{i}\Delta_{sp}}, \tag{5c}$$

and may simplify the interpretation of the Mueller matrix. Note that the subscripts sp and ps are interchanged with respect to the definition used by Schubert et al. [25].

It was also found useful, as in the work of Losurdo et al. [29], to interpret the data in terms of the (generalized) pseudo-dielectric function defined as [29]

$$\langle\varepsilon\rangle_{pp} = \varepsilon_0 \sin^2\theta_0 \left[1 + \frac{(1-\rho_{pp})^2}{(1+\rho_{pp})^2}\tan^2\theta_0\right]. \tag{6}$$

In Eq. (6), θ_0 denotes the polar angle of incidence, and ε_0 represents the dielectric function of the ambient.

4. Results and discussion

Figure 3 presents the elements of the normalized Mueller matrix recorded at $\theta_0 = 55°$ incidence (and $\theta_s = \theta_0$) with full azimuthal rotation of the sample. Since these data can be rationalized in the same way as the data for polar angles of incidence $\theta_0 = 45°$ and 65°, we will below only focus on the Mueller matrix measurements presented in Fig. 3. The elements of the Mueller matrix are presented as polar plots, where the azimuthal rotation angle (ϕ_0) is coded as the polar angle, and the radius represents the photon energy of the incident light (the inner circle corresponds to 0.73 eV and outer circle to 5.9 eV). The data are organized such that $\phi_0 = \angle(\mathbf{k}_\parallel, \mathbf{G}_\parallel^{(10)})$, where

$$\mathbf{k}_\parallel = k\sin\theta_0(\cos\phi_0, \sin\phi_0, 0) \tag{7}$$

represents the component of the incident wave vector parallel to the surface of the substrate [Fig. 2], and $\mathbf{G}_\parallel^{(10)}$ is the reciprocal lattice vector shown in Fig. 4. In writing Eq. (7), we have introduced the wave number in air, $k = \omega/c$ where $E = \hbar\omega$ is the energy of the incident light and c denotes the speed of light in vacuum. It is observed from Fig. 3 that the Mueller matrix of the sample is nearly block-diagonal for photon energies up till about 3 eV, which is as expected in terms of the Bedeaux-Vlieger model. Note that the m_{21} element is nominally identical to m_{12}, but we have on purpose chosen a different colorbar and rescaled m_{21} below 2.5 eV in order to better visualize the features weaker than the strong LSPR (see discussion below). A similar rescaling has also been applied to the m_{22} element. Finally, it is noted that the elements m_{34} and m_{43} are essentially equal in magnitude but have opposite signs, so that the Mueller matrix has the expected symmetry.

Figure 5 presents the corresponding ellipsometric angle ψ_{pp} [Fig. 5 left] and $\mathrm{Im}\langle\varepsilon\rangle_{pp}$ [Fig. 5 right] versus photon energy for azimuthal angles in the range 0° to 45° in steps of 5°. The LSPR is observed at around 2.1 eV, see Fig. 5, and corresponds to the inner circle in the block-diagonal elements of Fig. 3. The non-dispersive LSPR calculated using GranFilm is here defined by the maximum of the peak in $\mathrm{Im}\langle\varepsilon\rangle_{pp}$, and is represented by the inner circles in the elements m_{13} and m_{14} presented in Fig. 3. However, a small anisotropy at the plasmon resonance is readily observed in the off-block-diagonal elements surrounding the LSPR, and Fig. 5 shows clearly that the LSPR is slightly dispersive as a function of ϕ_0. The latter can also be

#240547 Received 7 May 2015; revised 3 Aug 2015; accepted 16 Aug 2015; published 21 Aug 2015

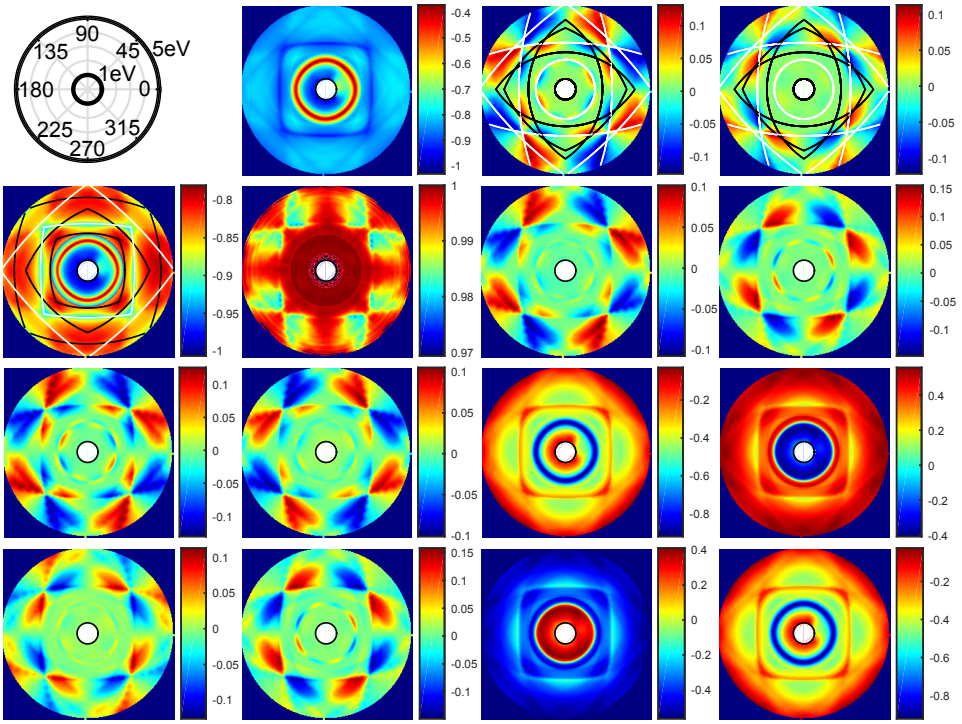

Fig. 3. Contour plots of the elements of the normalized Mueller matrix **m** for the sample shown in Fig. 1, measured for $\theta_0 = \theta_s = 55°$ (where θ_s denotes the polar scattering angle). The photon energy and the azimuthal rotation angle (ϕ_0) of the incident light represent the radius and the angle in these polar plots, respectively. The inner circle of the plots corresponds to the photon energy 0.73 eV, while the outer corresponds to 5.90 eV. The Rayleigh-lines for the first BZ (upright semi-square), the 2nd BZ (tilted semi-square) in air (white lines), and in the glass substrate (black lines) have been superimposed the m_{21} element. In the m_{13} and m_{14} elements, the extended Rayleigh-lines for air (white lines) and glass (black lines) that were calculated for a 90° symmetry are additionally superimposed, in addition to the LSPR resonance at 2.1 eV (white circles) as estimated from the quasi-static approximation. For reasons of improved visibility, the amplitudes of the elements m_{21} and m_{22} were reduced for E <2.5 eV; for this energy range, $\mathrm{sgn}(m_{2j})|m_{2j}|^{1/4}$ was presented for $j = 1,2$ where $\mathrm{sgn}(\cdot)$ denotes the signum (or sign) function. The circles in the schematic inset, replacing the m_{11} element (that is trivially one), correspond to photon energy of the incident light from 1 eV (thick inner line) to 5 eV (thick outer line) in steps of 1 eV, while 0, 45, 90, etc. denote the azimuthal rotation angle (ϕ_0) in degrees.

#240547 Received 7 May 2015; revised 3 Aug 2015; accepted 16 Aug 2015; published 21 Aug 2015

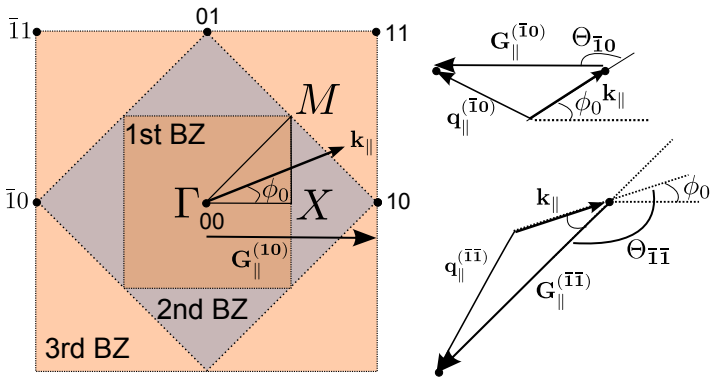

Fig. 4. Schematic diagram of the reciprocal square lattice, where the experimental azimuthal angle is defined by the angle ϕ_0 between the vectors $\mathbf{k}_\parallel$ and $\mathbf{G}_\parallel^{(10)}$; $\phi_0 = \angle(\mathbf{k}_\parallel, \mathbf{G}_\parallel^{(10)})$. The boundaries of the 1st, 2nd, and 3rd BZs are indicated by dotted lines, and the high symmetry points are shown. The Bragg conditions for the first and the third BZs are indicated for $\phi_0 \leq 45°$, with $\Theta_\mathbf{m} = \phi_\mathbf{m} - \phi_0$.

observed by a careful inspection of the LSPR in the block-diagonal elements of Fig. 3, as the LSPR is seen to be deformed from the circular shape.

For energies above approximately 3 eV, complex patterns are found in all Mueller matrix elements. This is principally a result of the photonic crystal character of the lattice, but possibly also a result of coupling to collective plasmon (CP) modes. Indeed, a careful inspection of the experimental data in Fig. 3 show that it is possible to directly extract both the Brillouin zone (BZ) of the reciprocal lattice, and thus with high accuracy the lattice parameters. This is in principle similar to the extraction of the band-diagram from p- and s-polarized reflection data from metallic photonic crystals, as described in detail by Giessen et al. [6], while the ability of spectroscopic ellipsometry to observe the Rayleigh-anomalies for a grazing diffracted beam (hereby referred to as the Rayleigh-lines) has also been reported [13, 30, 31]. As we mainly determine the specular peak in spectroscopic ellipsometry, what is observed is thus the indirect effect of the grazing diffracted waves [13].

4.1. Rayleigh-lines

We will now show that the main features of the Mueller matrix for photon energies above the LSPR energy can be described by estimating the Rayleigh-line, i.e. the condition for a scattered or transmitted wave vector along the surface [6, 13]. In particular, it will become clear from the discussion below that the sharp dip in the m_{21}=m_{12} elements (or the dip in $\mathrm{Im}\,\langle\varepsilon\rangle_{pp}$) conveys the Rayleigh-line for a grazing diffracted wave along the surface, but in air. Due to the transparent substrate, the Rayleigh-line for a grazing diffracted beam in the transparent glass substrate is also easily observed.

Let us start our discussion by defining the diffracted wave vector into the air or glass by [32]

$$\mathbf{q}_\parallel^{(\mathbf{m})} = \mathbf{k}_\parallel + \mathbf{G}_\parallel^{(\mathbf{m})}, \tag{8}$$

where the two-dimensional reciprocal lattice vectors are

$$\mathbf{G}_\parallel^{(\mathbf{m})} = m_1\mathbf{b_1} + m_2\mathbf{b_2} = G_\parallel^{(\mathbf{m})}\left(\cos\phi_\mathbf{m}, \sin\phi_\mathbf{m}, 0\right). \tag{9a}$$

Here $\mathbf{m} = (m_1, m_2)$ with m_1 and m_2 integers, while $\mathbf{b_1}$ and $\mathbf{b_2}$ denote the primitive translation vectors of the reciprocal lattice ($|\mathbf{b_{1,2}}| = 2\pi/a$). In the last transition of Eq. (9a), the reciprocal

#240547 Received 7 May 2015; revised 3 Aug 2015; accepted 16 Aug 2015; published 21 Aug 2015

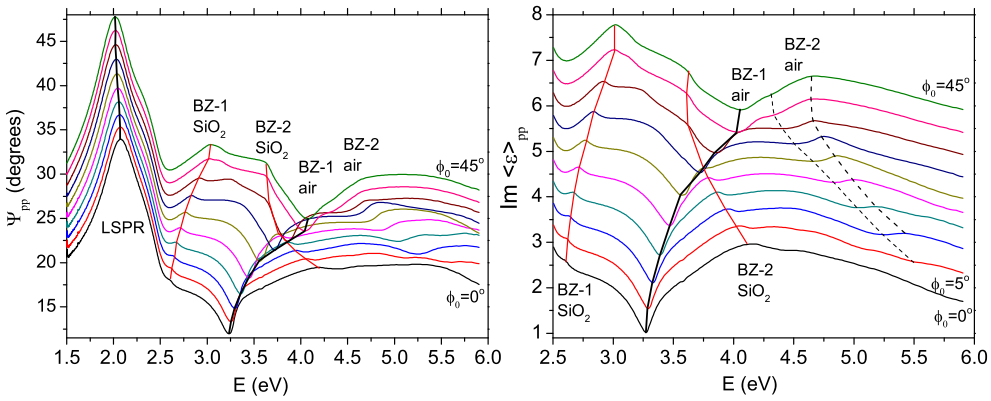

Fig. 5. The energy dependence of ψ_{pp} in the range 1.5–5.9 eV (left); and $\mathrm{Im}\langle\varepsilon\rangle_{pp}$ in the range 2.5–5.9 eV (right), for azimuthal angles of incidence from $\phi_0 = 0°$ (incidence along Γ-X) to $\phi_0 = 45°$ (incidence along Γ-M) in steps of $\Delta\phi_0 = 5°$. The dispersion of the LSPR can be seen in ψ_{pp} around 2.1 eV. Three approximate Rayleigh-lines are drawn by hand in both sub-figures, while the location of the BZ-2 in air is more ambiguous. For clarity, the ψ_{pp}-curves were offset by $1.4°\kappa$ and the $\mathrm{Im}\langle\varepsilon\rangle_{pp}$-curves by 0.2κ where $\kappa = \phi_0/\Delta\phi_0$.

lattice vector has been expressed in polar coordinates in terms of its length, which for a square lattice is ($\mathbf{b_1} \perp \mathbf{b_2}$)

$$G_{\parallel}^{(\mathbf{m})} = \left|\mathbf{G}_{\parallel}^{(\mathbf{m})}\right| = \frac{2\pi}{a}[m_1^2 + m_2^2]^{1/2}, \tag{9b}$$

and the angle $\phi_{\mathbf{m}}$. The Rayleigh-line condition [6] for a grazing diffracted wave is defined by $\mathbf{q}_{\parallel}^{(\mathbf{m})} = \mathbf{q}^{(\mathbf{m})}$, which implies that

$$\left|\mathbf{q}_{\parallel}^{(\mathbf{m})}\right|^2 = n_i^2 k^2, \tag{10}$$

where n_i is the refractive index of the ambient (air) or the substrate (SiO_2). The equation determining all Rayleigh-lines follows directly from Eqs. (7)–(10), and when it is assumed that the light is incidence from air ($n_i = 1$), it takes the form

$$k^2 - \frac{2k\sin\theta_0 G_{\parallel}^{(\mathbf{m})}\cos(\phi_{\mathbf{m}} - \phi_0)}{n_i^2 - \sin^2\theta_0} - \frac{\left(G_{\parallel}^{(\mathbf{m})}\right)^2}{n_i^2 - \sin^2\theta_0} = 0. \tag{11}$$

To understand the meaning of Eq. (11), we start by referring to Fig. 4 and assuming for simplicity that $\phi_0 \in (0°, 45°)$. Under these circumstances, setting $\mathbf{G}_{\parallel}^{(\mathbf{m})}$ equal to $\mathbf{G}_{\parallel}^{(\bar{1}0)}$ and $\mathbf{G}_{\parallel}^{(\bar{2}0)}$ in Eq. (11) will give the boundary of the 1st and the 3rd BZ, respectively; similarly, setting the reciprocal lattice vectors equal to $\mathbf{G}_{\parallel}^{(\bar{1}\bar{1})}$ gives the boundary of the 2nd BZ. Note that a single measurement using focusing probes causes a spread in $\mathbf{k}_{\parallel}$, hence the broadening of the peaks and dips are partially a result of the focusing optics used in the current experiment (in addition to the resolution of the spectrograph) [13].

For given angles of incidence (θ_0, ϕ_0), solving Eq. (11) with respect to k results in the various Rayleigh-lines that are overlaid the m_{21}, m_{13} and m_{14} elements of Fig. 3. It is observed that the dips in m_{21} follow the boundaries of the 1st and 2nd BZ with $n_i = 1$ (grazing wave in air). The latter implies that one may observe a similar dip in ψ_{pp}, as further shown in the left Fig. 5 and

#240547 Received 7 May 2015; revised 3 Aug 2015; accepted 16 Aug 2015; published 21 Aug 2015

bottom Fig. 6. The other block-diagonal elements, e.g. m_{33} and m_{44} show also quite clearly these boundaries.

The pseudo-dielectric function $\mathrm{Im}\langle\varepsilon\rangle_{pp}$ was found to convey particularly strongly the Rayleigh-lines in addition to the dispersive LSPR, as shown in the right Fig. 5 and the contour plot in the top Fig. 6. It is further easy to extract numerically these boundaries directly from the data, as seen in Fig. 5. Indeed, a close inspection of Fig. 5 shows that the strong dips for the 1st BZ with $n_i = 1$, in both $\mathrm{Im}\langle\varepsilon\rangle_{pp}$ and ψ_{pp}, indicate that it is mainly the p-polarized light that is coupled into the grazing diffracted mode. The strong peaks at the 1st BZ with $n_i = 1.47$ (grazing wave in glass) are thus the results of either an enhanced p- or a reduced s-reflectance of the specularly reflected beam at the condition of a grazing diffracted wave. A similar, but weaker behavior can be observed on the boundaries of the 2nd BZs, i.e. the weak dip at the boundaries of the 2nd BZ in air and the weak peak at the boundaries of the 2nd BZ in glass.

Note that k in Eq. (11) can be obtained by a direct readout of the energy location of the strong dip in $\mathrm{Im}\langle\varepsilon\rangle_{pp}$ or ψ_{pp}. Further, the correspondence between Eq. (11) and the experimentally observed dip, appears closest near the X point in the first BZ. Thus, solving Eq. (11) for the lattice constant, using the experimentally obtained k value near the X point, results in a sensitivity and precision of a few Ångströms, since no dispersive refractive index is involved. However, in our data, the energy positions of the minimum of ψ_{pp} and the minimum of $\mathrm{Im}\langle\varepsilon\rangle_{pp}$ differ slightly, and this ambiguity must be resolved by further numerical calculations for an absolute accuracy. Similarly, the refractive index of the substrate may be determined in a limited spectral range by solving Eq. (11) for n_{glass} given one or several of the Rayleigh-lines for glass obtained experimentally (and the experimental parameters under which they were obtained).

It is observed that the strong peaks in m_{12}, and the broader peaks in $\mathrm{Im}\langle\varepsilon\rangle_{pp}$ and ψ_{pp}, follow the Rayleigh-line for the 1st BZ with $n_i = 1.47$. The amplitudes of these peaks are clearly enhanced at the M point, i.e. for $\phi_0 = 45°$ in Figs. 3 and 5. To investigate these resonances further, Fig. 6 presents contour plots of $\mathrm{Im}\langle\varepsilon\rangle_{pp}$ [Fig. 6 top] and ψ_{pp} [Fig. 6 bottom] as functions of ϕ_0 and the energy of the incident light. Moreover, in this figure, the Rayleigh-lines for the 1st and 2nd BZ in air (white lines) and the substrate (black lines) are also indicated. It is observed from Fig. 6 that $\mathrm{Im}\langle\varepsilon\rangle_{pp}$ is resonantly enhanced at the corners of the BZs in glass, i.e. a strong peak at the M point (in the corners of the 1st BZ) at energy $E_{R1} = 3.08\,\mathrm{eV}$, and a weaker, but broader peak at the X point (in the corners of the 2nd BZ) at $E_{R2} = 4.15\,\mathrm{eV}$. Both peaks are accompanied by an enhanced total reflected intensity (results not shown), proportional to the M_{11} element in Eq. (2). As a consequence, the enhancement of ψ_{pp} can be deduced to be mainly a result of an enhancement of the amplitude of the p-polarized component of the reflected light, which appears to be in reasonable correspondence with Kravets et al. [13], although the dependency on the azimuthal incidence angle ϕ_0 is not reported in their work. In our work, these resonances additionally take place in the region dominated by the interband transitions of gold, i.e. around the local maxima of $\mathrm{Im}\{\varepsilon_{\mathrm{Au}}\}$ around 3.3 eV and 4.5 eV, and the cut-off shape of $\mathrm{Im}\langle\varepsilon\rangle_{pp}$ between 3.5 eV and 3.8 eV appears correlated to maxima in the polarizability component normal to the surface, as calculated using GranFilm and the procedure outlined by Lazzari et al. [22, 33].

The dips in ψ_{pp} observed experimentally [Fig. 6 bottom], deviate from the Rayleigh-lines at the M point for BZ-1 and at the X point for BZ-2, which we here regard as the opening of the photonic gap. Furthermore, let us define the extended Rayleigh-lines, as those calculated from Eq. (11) for e.g. $45° \leq \phi_0 \leq 90°$ using $\mathbf{G}_{\parallel}^{(\bar{1}0)}$. These extended Rayleigh-lines do not correspond to a dip in ψ_{pp}, but rather a boundary (edge) of the regions with peaks, as discussed above. This is visualized by the dashed lines in Fig. 6, and is particularly well observed in ψ_{pp}. Giessen et al. [6] argue strongly that at least the Rayleigh-lines in air are properties of the photonic crystal

#240547 Received 7 May 2015; revised 3 Aug 2015; accepted 16 Aug 2015; published 21 Aug 2015

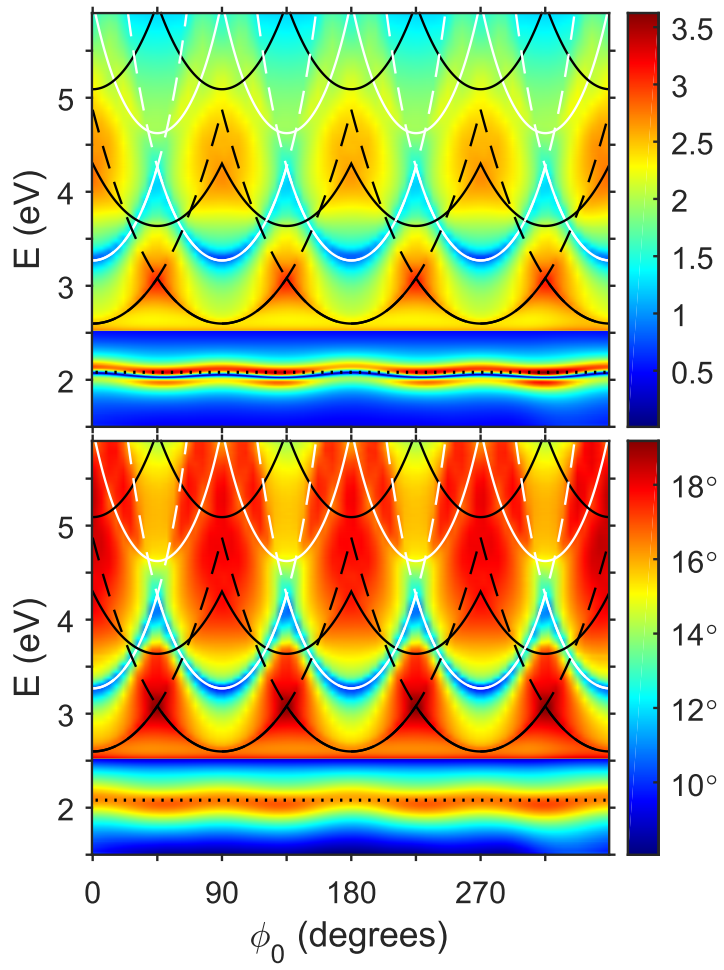

Fig. 6. Contour plots of the variations of $\mathrm{Im}\langle\varepsilon\rangle_{pp}$ (top) and ψ_{pp} (bottom) with azimuthal angle ϕ_0 and photon energy E. In both sub-figures, the Rayleigh-lines corresponding to the 1st and the 2nd BZ in air (white lines), and in the substrate (black lines), have been indicated. The horizontal black dotted lines seen abound 2.1 eV correspond to the position of the LSPR obtained by GranFilm [21]. For better visibility, a scaling has been applied for photon energies below 2.5 eV so that the plotted quantities are $\mathrm{Im}\langle\varepsilon\rangle_{pp}/5.6$ (top) and $\psi_{pp}/2$ (bottom).

#240547
Received 7 May 2015; revised 3 Aug 2015; accepted 16 Aug 2015; published 21 Aug 2015

character of such a surface. Their argument is based on comparisons to simulations of dielectric 2D photonic crystals on glass [6].

4.2. *Dispersion of the polarization coupling*

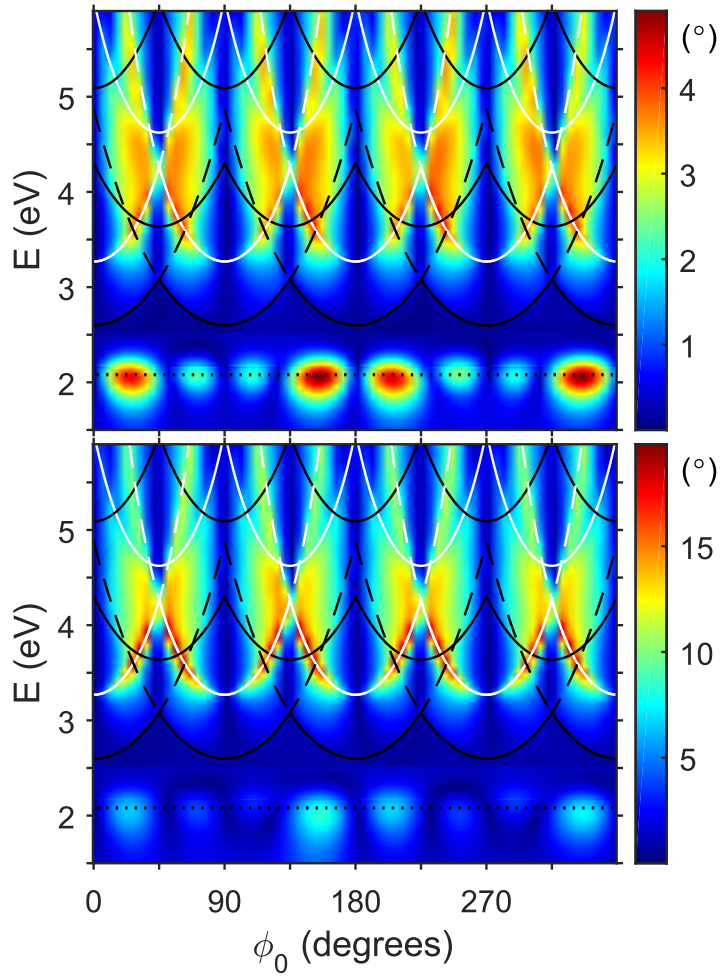

Fig. 7. Contour plots of the ellipsometric angles ψ_{ps} (top) and ψ_{sp} (bottom) with azimuthal angle ϕ_0 and photon energy E. In both sub-figures, the Rayleigh-lines corresponding to the 1st and the 2nd BZ in air (white lines), and in the substrate (black lines), have been indicated. The horizontal black dotted lines seen around 2.1 eV correspond to the energy position of the LSPR obtained by GranFilm [21]. For reasons of improved visibility, ψ_{ps} and ψ_{sp} are scaled by 2 for E <2.5 eV.

We now focus on the polarization coupling observed through the non-zero signals in the off-block-diagonal elements in Fig. 3. The Mueller matrix elements of this figure represent the raw measurements and can be used to calculate the recorded intensity with e.g. crossed polarizers, but interpretation involves both phase and amplitude. The effect of polarization conversion, that is, cross-polarized specularly reflected light, may perhaps be more easily conveyed by inspecting ψ_{sp} quantifying the conversion from p-polarized incident light into s-polarized scattered light, and ψ_{ps} representing conversion of s-polarized into p-polarized light. Figure 7 presents

#240547 Received 7 May 2015; revised 3 Aug 2015; accepted 16 Aug 2015; published 21 Aug 2015

contour plots of the ellipsometric angles ψ_{ps} (top) and ψ_{sp} (bottom) as functions of energy and azimuthal rotation angle, ϕ_0, where $\phi_0 \in (0°, 45°)$ corresponds to the first BZ for the square lattice. The Rayleigh-lines are plotted in Fig. 7 as white (air) and black (glass) lines, while the dotted black horizontal lines in the same figure correspond to the main non-dispersive LSPR estimated from GranFilm. The results of Fig. 7 show that the polarization coupling follows to a large extent the above described extended Rayleigh-lines (i.e. also including the dashed white lines), with three important exceptions. First, only the Rayleigh-lines in air are observed. Secondly, there are strong polarization couplings around the LSPR energy and near the azimuthal angles $\phi_0 = 22.5°$, $67.5°$ and so on. Finally, there are two cones extending toward higher photon energies, near the M point in the BZ. These cones follow the extended Rayleigh-lines, only observed as boundaries in Fig. 6, and have a reduced symmetry compared to the square lattice. Indeed, it is also noted based on the amplitudes near the LSPR, that the sample has a 90° symmetry, i.e. a folding can be done along the dark blue vertical sections of Fig. 7.

These extended Rayleigh-lines reproduce the main features of the off-bock-diagonal elements in the measured Mueller matrix in Fig. 3, as is shown by the calculated white (air) and black (glass) lines plotted in the m_{13} and m_{14} elements. However, from Fig. 7 it is more obvious to observe how the above cones appear to extrapolate through the crossing point at the M-point, through the polarization coupling around the LSPR. The dispersion of the polarization coupling appears thus to share certain features with the Dirac cones appearing for reduced symmetries, such as two-dimensional hexagonal lattices [34] and particularly line centered square lattices [35]. We speculate that the reduced symmetry of the dispersion of the polarization coupling is at the origin of such "Dirac-like" cones in Fig. 7.

It appears necessary to resort to numerical simulation techniques to quantifying the polarization coupling phenomena and fully understand the response of metallic/plasmonic photonic crystals and the coupling to collective plasmons/photonic crystal modes and surface plasmons. As such, the Rigorous Coupled Wave Analysis (RCWA) [36] has been demonstrated to be suitable to model the specular Mueller matrix for various semiconductor cylinders [37], and recently fully rigorous boundary element or surface integral methods have been developed [38, 39]. Moreover, the moderate aspect ratio of the hemispheroidal particles considered in this study may allow for using (approximate) numerical methods, for instance, the reduced Rayleigh equation technique [27,32,40]. This latter technique also has the additional advantage of being well suited for studying the optical effects of sample imperfections caused by *e.g.* non-periodicity and/or the particles not all being of the same shape and size. We also note that recent numerical simulations using Dirichlet-to-Neumann maps to calculate the electric and magnetic field densities for square lattices of metallic rods [41] and metamaterial rods [42] revealed resonant modes in the field components that appear to have a similar symmetry to those observed here for the polarization coupling around the LSPR.

5. Summary and Conclusions

Focused Ion Beam milling of Au on uv-transparent glass substrates, supplies a fundamental research point for studying the far field spectroscopic specular Mueller matrix of metallic/plasmonic photonic crystals. The system studied in this work, consists of a square lattice of Au hemispheroidal particles supported by a glass substrate where the lattice constant is 210 nm, the height of the gold particles is 25–30 nm, and their lateral radius is (54 ± 4) nm. For this system, it is observed that for energies below 3.3 eV the Mueller matrix response can reasonably well be understood within the quasi-static approximation. However, the peak position of the LSPR is slightly dispersive as a function of azimuthal rotation angle, and a weak polarization coupling can be observed surrounding the LSPR; both these effects are found to be caused by the lattice.

#240547 Received 7 May 2015; revised 3 Aug 2015; accepted 16 Aug 2015; published 21 Aug 2015

At higher energies, the lattice contribution is found to play an even more important role. A sharp dip in ψ_{pp} and in $\mathrm{Im}\langle\varepsilon\rangle_{pp}$ corresponding to the Rayleigh-line (grazing wave in air) allows for, in principle, the determination of the lattice parameters with sub-nanometer accuracy. On the other hand, the Rayleigh-lines corresponding to grazing waves in the substrate result in peaks that become resonant at the M point for the first Brillouin zone and at the X-point for the second Brillouin zone. Strong off-block-diagonal elements appear at energy locations surrounding or at the Rayleigh anomalies due to grazing Bragg waves in air or in the substrate, but the dispersion of this polarization coupling appears as multiple "Dirac-like" cones, all with a 90° symmetry rather than the 45° symmetry of the square lattice. A computational study appears necessary in order to unambiguously determine the origin of the observed features in the complete Mueller matrix, with respect to coupling to photonic crystal modes and collective plasmon modes.

Acknowledgment

The authors are grateful to John Walmsley at SINTEF for help with the SEM images, Astrid Bjørkøy at NTNU for the AFM images, and the NTNU Nanolab staff for guidance in sample manufacturing. Moreover, Z.G. acknowledges funding from NORFAB for access to NTNU Nanolab during the year 2013. The research of I.S. was supported in part by The Research Council of Norway Contract No. 216699.

#240547 Received 7 May 2015; revised 3 Aug 2015; accepted 16 Aug 2015; published 21 Aug 2015